International Journal of Mechanical Sciences 51 (2009) 682–693

Contents lists available at ScienceDirect

International Journal of Mechanical Sciences

journal homepage: www.elsevier.com/locate/ijmecsci

Improved analysis of the modified split-cantilever beam for mode-III fracture

András Szekrényes *

Department of Applied Mechanics, Budapest University of Technology and Economics, 1111 Budapest, Muegyetem rkp. 3-5, Building MM, Hungary

ARTICLE INFO

Article history:
Received 24 October 2008
Received in revised form
28 July 2009
Accepted 31 July 2009
Available online 6 August 2009

Keywords:
Interlaminar fracture
Mode-III delamination
Modified split-cantilever beam
Composite specimen
Experiment
Beam theory

ABSTRACT

A closed-form solution for the compliance and the energy release rate of the updated version of the mode-III split-cantilever beam specimen is developed incorporating linear beam theories. Apart from bending and shear of the specimen, the Saint-Venant and free torsion effects are considered. The analytical solution is verified by finite element calculations, leading to the conclusion that the compliance is very accurately determined, while the energy release rate differs only with 5% compared to the finite element calculations. Based on the finite element analysis the recommended crack length range is given in order to design a configuration that gives 98% mode-III contribution to the total energy release rate. At the final stage the analytical model is applied to reduce the data from experiments performed on delaminated glass/polyester composite beams. The results show that the closed-form solution is in a very good agreement compared to the results by experiments, although this requires very accurate measurements.

1. Introduction

In the last decade more and more attention was focused on the investigation of mode-III interlaminar fracture mechanisms of laminated composite materials. This indicates that – apart from the mode-I and mode-II fractures - mode-III is important too for the complete fracture characterization of the material. However, mode-III fracture involves several difficulties, which do not take place under mode-I, mode-II and mixed-mode I/II tests. One of them is that – to the best of the author's knowledge – a pure mode-III fracture cannot be produced.

Similar to mode-I and mode-II delaminations there are several – more or less effective – test methods to measure the fracture toughness of the material under mode-III loading. The crack rail shear (CRS) [1] specimen produces very low compliance values, so the compliance calibration (CC) method cannot be applied for data reduction. Furthermore, the energy release rate (ERR) in the CRS specimen has a significant mode-II component and the double precracks do not propagate simultaneously. Also, one of the earliest developments is the split-cantilever beam (SCB) [2], which incorporates the loading parallel to the delamination plane. The method was applied by numerous authors [3–5]. Later, it has been shown that mode-II component in the SCB specimen is significant: it is more than 40% of the total energy release rate [3]. On the other hand the distribution of the ERR (both mode-II and mode-III) is non-uniform: a dramatic variation exists along the crack front. Therefore, the split-cantilever beam rather produces a mixed-mode II/III cracking and the mode ratio varies significantly along the crack front. In order to eliminate the significant mode-II component the specimen was loaded using very stiff blocks, see for example the work by Hwang and Hu [5]. However, this way the beam theory cannot be applied in a simple way to reduce the experimental data. Robinson and Song [6] proposed the loading scheme necessary to reduce the mode-II component; while implementing their idea, Sharif et al. [3] and Trakas and Kortschot [7] constructed a special rig realizing a mode-III dominant fracture. The method was applied recently by Rizov et al. [8] to test glass fiber-reinforced woven laminates including finite element analysis and experiments.

The edge-crack torsion (ECT) specimen was developed by Lee [9]. It is considered as a very important contribution to mode-III fracture developments [10–13]. An important feature of the ECT specimen is that the compliance calibration (CC) method can be applied [9]. Although the effect of friction in the ECT test was proven to be insignificant [13] in a recent study, Ratcliffe [15] showed some drawbacks of the test, like the dependence of the ERR on the crack length, the deviation of the load–displacement curves from linearity and the damage of the specimen before delamination failure. Recently, the ECT test was applied by Pennas and Cantwell [16], who showed (corresponding with the results with Ratcliffe [15]) that the mode-III ERR increases with crack length.

The anti-clastic plate bending (ACPB) was originally applied to determine the in-plane shear modulus of various materials. Later it was found to be an efficient tool for the determination of mode-III fracture toughness [17]. The method uses a rectangular plate

* Tel.: +36 1 463 1170; fax: +36 1 463 3471.
E-mail address: szeki@mm.bme.hu

0020-7403/$ - see front matter © 2009 Elsevier Ltd. All rights reserved.
doi:10.1016/j.ijmecsci.2009.07.005

with side grooves in the middle line of the plate. Due to the side grooves the APCB produces a pure in-plane shear field. In the work of Podczek [18] it has been shown that the critical stress intensity factor (of a pharmaceutical powder compact material) decreases significantly with notch depth of the APCB specimen. The extension of the method for combined modes and several materials is in progress [18].

Ehart et al. [19,20] applied a splitting specimen for the fracture characterization of wood material including mode-I, mode-II and mode-III loadings. The specimen is similar to that applied in the compact tension (CT) test for mode-I fracture investigation [21]. The relative drawbacks of the test are that it requires difficult specimen geometry and the ERR rate can be evaluated only by using the finite element method.

The mode-III version of the four point-bend end-notched flexure ($4ENF_{III}$) specimen was investigated by Yoshihara [22]; however, it was applied to measure the R-curve of wood. Although the $4ENF_{III}$ provides a 90% mode-III test, the specimen contains two parallel cracks (growing simultaneously), requires side grooves along the longitudinal direction and involves relatively large specimen dimensions. Hence, it does not seem to be an optimal solution for composites, especially for glass fiber-reinforced composites, where the side grooves are difficult to be made, because the hardness of the glass fiber is approximately equal to that of the milling tool.

The aim of the present work is to improve the efficiency of the MSCB specimen, to provide an accurate closed-form solution for the compliance and the energy release rate [3,7] and to demonstrate its applicability for the reduction of experimental data. The MSCB specimen maintains the traditional beam-like geometry. Another reason for developing closed-form solution and performing experiments is that it is possible to combine it with mode-I double-cantilever beam (DCB) [23] and mode-II end-notched flexure test (ENF) [24,25]. In a recent work the prestressed end-notched flexure (PENF) fracture specimen was introduced for mixed-mode I/II loading [26]. Although the test has several drawbacks, its simplicity is a great advantage. A study based on the combination of the ENF-MSCB specimens – leading to a mixed-mode II/III fracture mechanical system – has been published recently in the literature [27].

2. Modification of the original MSCB configuration

The load transfer of the MSCB specimen is demonstrated in Fig. 1. The two rigs transfer a scissoring load to the specimen. Compared to the rig used in [3,7] substantial modifications were made. The surface of the rigs was grooved and two steel rollers were inserted, holding the specimen in a given sideways (y) position (see Fig. 1). This way it was possible to eliminate entirely the crack opening, which would induce a substantial increase in the mode-I ERR component. Furthermore the loading rollers applied by Sharif et al. [3] were substituted with grub screws, which made it very easy to control and hold the loads in the right position by using a screwdriver. Finally, the twisting of the specimen is enabled (in contrast with the original rig), which involves the consideration of the free torsion effect in the specimen.

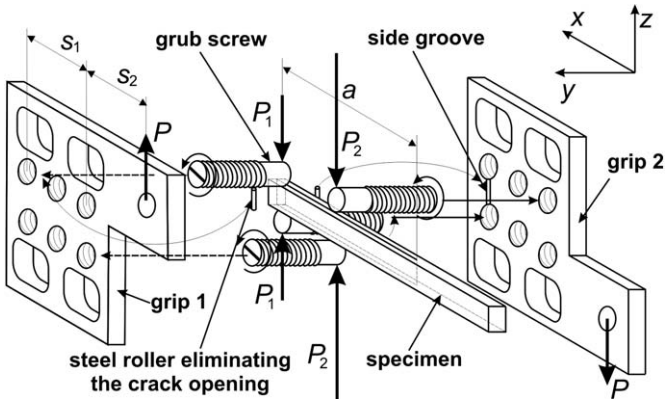

Fig. 1. Exploded view of the mofified split-cantilever beam.

The 3D view of the applied equipment and the most important details are given in Fig. 2 developed in SOLIDWORKS. The load was transferred by the load transferring plates, which were held in a given sideways position using the wedge loading blocks of the testing machine. The blocks were inserted to the loading plates, preventing the rotation around axis x and the displacement in the y direction of the loading plates. The loading grips are free to rotation around the y axis using the shafts shown in Fig. 2. Since the plates transfer two loads involving non-coinciding influence lines, the distance between them produces a moment about the x axis. This moment is completely transferred to the shafts and in fact the specimen is loaded only by forces (P_1 and P_2) through the four grub screws. The friction between the welded tube and the shaft was assumed to be negligible and both were lubricated with grease. Using this equipment it is possible to reduce the load of the specimen to a beam problem subjected to basic types of load.

3. Analysis

In Fig. 3 there are two different distances, s_1 and s_2, that determine the loads of the specimen. An important feature of the rig provided in [3,7] is that the external load of the upper and lower grips transferred by roller C should lie in the same y position in order to ensure the moment equilibrium. In our equipment this requirement is eliminated due to the very stiff load transferring plates. The force and moment equilibrium at roller C involve (see Fig. 3)

$$P_1 = P\frac{s_2}{s_1}, P_2 = P\left(1+\frac{s_2}{s_1}\right), \tag{1}$$

where P is the external load at roller C. Rollers A and B should span the thickness of the specimen arms (h); this way the rollers transfer a uniformly distributed load along the thickness involving a resultant force at $h/2$ distance from the specimen boundary. In the following we treat the specimen arm as a cantilever beam (Fig. 4). We consider five deformations: bending, shearing, Saint-Venant effect, and twisting of the specimen arms, respectively.

3.1. Simple beam theory

The application of the Euler–Bernoulli beam theory to the MSCB specimen is relatively simple, see e.g. [25]. Based on Fig. 4a the displacements from bending at the points of load applications are

$$\delta_{1EB} = \frac{2P(2a^3+(s_1+s_2)(s_1^2-3a^2))}{b^3hE_{11}}, \tag{2}$$

$$\delta_{2EB} = \frac{2P(6as_1(s_1+s_2)-s_1^2(2s_1+3s_2)-a^2(6s_1+3s_2-2a))}{b^3hE_{11}}, \tag{3}$$

where P is the applied load, a is the crack length, s_1 and s_1 are the distances between the loading rollers A, B and C, respectively, b is the specimen width, h is half of the specimen thickness and E_{11} is the flexural modulus of the material.

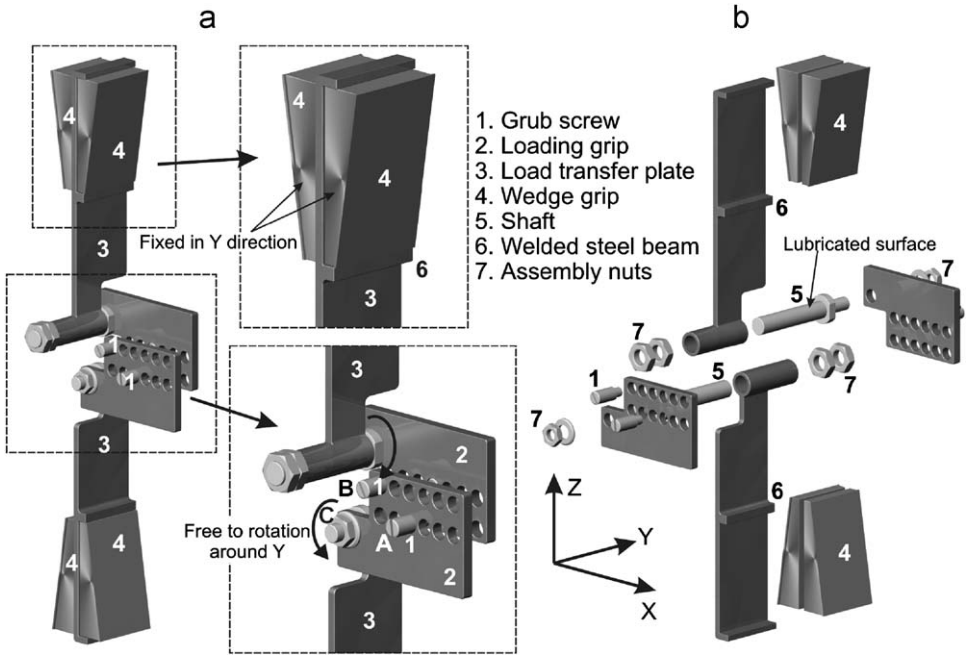

Fig. 2. The 3D view of the experimental equipment. Assembled state (a) and exploded view(b).

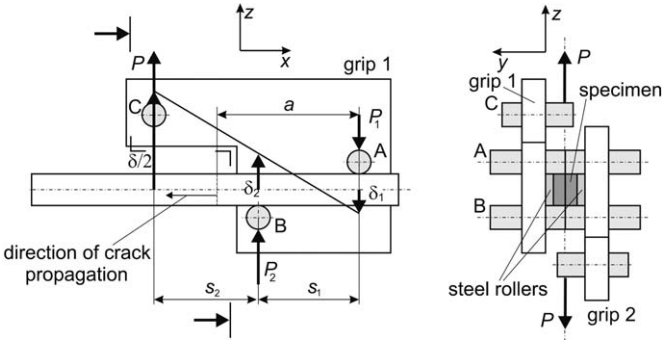

Fig. 3. Schematic illustration of the MSCB specimen.

3.2. Timoshenko beam theory

It will be shown later that the effect of transverse shear on the ERR is significant. Following the way shown, e.g. by Ozdil et al. [25], and using again Fig. 4a the displacements from transverse shear are

$$\delta_{1TIM} = \frac{P(a - s_1 - s_2)}{bhkG_{13}}, \tag{4}$$

$$\delta_{2TIM} = \frac{P(a - s_1)}{bhkG_{13}}, \tag{5}$$

where $k = 5/6$ is the shear correction factor and G_{13} is the shear modulus in the x–z plane, respectively.

3.3. Saint-Venant effect

The Saint-Venant effect represents an angle of rotation at the cross-section lying in the $x = 0$ plane (Fig. 4b). Olsson considered this effect in the case of the mode-I double-cantilever beam specimen (DCB) [23]. According to Olsson's analysis the strain energy derivative in the coordinate system in Fig. 4b is bounded by the following inequality:

$$\frac{\partial U}{\partial x} \le 2\frac{\partial U}{\partial x}|_{x=0} e^{-(2x/\kappa)}, \kappa = \frac{b}{2\pi}\left(\frac{E_{11}}{G_{13}}\right)^{1/2}, \tag{6}$$

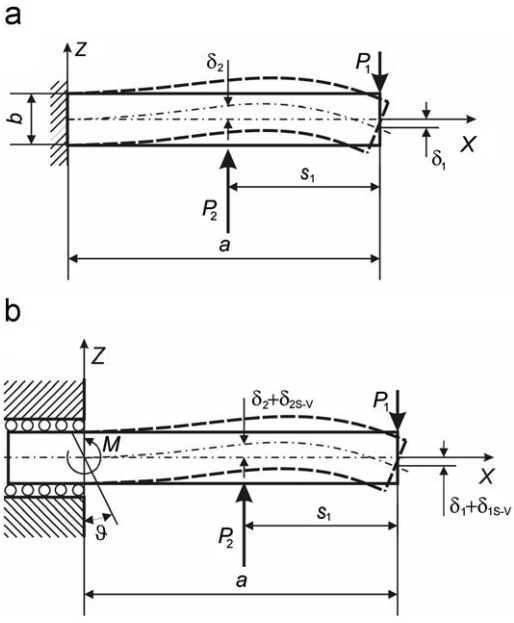

Fig. 4. The cantilever beam model of the MSCB specimen (a). The Saint-Venant effect at the clamped end (b).

where U is the strain energy, κ is the characteristic decay length in the material,

$$\left(\frac{\partial U}{\partial x}\right)|_{x=0} = \frac{1}{2} I_{y1} E_{11} (w''|_{x=0})^2 = \frac{1}{2}\frac{M^2}{I_{y1}E_{11}} = \frac{6M^2}{b^3 h E_{11}}, \tag{7}$$

$$U \le \int_0^\infty 2\left(\frac{\partial U}{\partial x}\right)|_{x=0} e^{-(2x/\kappa)}\, dx = \frac{12M^2}{b^3 h E_{11}} \int_0^\infty e^{-(2x/\kappa)}\, dx$$

$$\Rightarrow U_1 \le \frac{6M^2\kappa}{b^3 h E_{11}}, \tag{8}$$

where $I_{y1} = b^3 h/12$. In the following we consider the lower sign in Eqs. (6) and (8). Using Castigliano's second theorem and adopting

the lower sign we obtain the rotational angle at $x=0$

$$\vartheta = \frac{\partial U}{\partial M}. \tag{9}$$

The bending moment at $x=0$ is $M=P(a-s_1-s_2)$. Thus, the rotational angle by using Eq. (8) is

$$\vartheta = \frac{12M\kappa}{b^3hE_{11}} = \frac{12P(a-s_1-s_2)\kappa}{b^3hE_{11}}. \tag{10}$$

At the points of load application the angle of rotation causes the following displacement increments (note that the second of Eq. (6) is incorporated):

$$\delta_{1S-V} = \vartheta \cdot a = \frac{12P(a-s_1-s_2)a\kappa}{b^3hE_{11}} = \frac{6P(a-s_1-s_2)a}{b^2hE_{11}\pi}\left(\frac{E_{11}}{G_{13}}\right)^{1/2}, \tag{11}$$

$$\delta_{2S-V} = \vartheta(a-s) = \frac{12P(a-s_1-s_2)(a-s_1)\kappa}{b^3hE_{11}} = \frac{6P(a-s_1-s_2)(a-s_1)}{b^2hE_{11}\pi}\left(\frac{E_{11}}{G_{13}}\right)^{1/2}. \tag{12}$$

It should be mentioned that according to Fig. 4b both displacements (at rollers A and B) are positive. It is also obvious that actually the distribution of axial displacements at $x=0$ is not linear, like it is shown in Fig. 4b, because at the crack front they should be zero, and there is some nonlinear variation along both the y and z directions, respectively.

3.3. Free torsion of orthotropic beams

The torsion of orthotropic beams was analyzed by Timoshenko and Goodier [28], Liao and Sun [13] and Zhao and Wang [14], while Sankar [29] investigated the torsion of laminated composite beams. The load of the specimen requires the investigation of the torisonal problem in the MSCB specimen. In the work by Sharif et al. [3] the twisting of the specimen was eliminated using very stiff blocks. Here we consider the case when the specimen twisting is enabled; the problem is depicted in Fig. 5a. The angle of twist causes a relatively small displacement of the center (c_1) of the cross-section depicted in Fig. 5b. The problem can be treated as a free beam loaded with torsional moments at the ends shown by Fig. 5c. The determination of the angle of twist requires the solution of the boundary value problem for the torsion of orthotropic beams [12,13]:

$$\frac{1}{G_{13}}\frac{\partial^2\Psi}{\partial y^2} + \frac{1}{G_{12}}\frac{\partial^2\Psi}{\partial z^2} = -2\theta, \tag{13}$$

$$\Psi|_g = 0, \tag{14}$$

where $\Psi(y,z)$ is the Prandtl stress function, G_{13} is the shear modulus in the x–z plane and θ is the angle of twist per unit length of beam. The solution for isotropic beams with rectangular cross-section was provided by Timoshenko and Goodier [28]. In a similar way it can be developed also for orthotropic cross-sections:

$$\Psi(y,z) = 2G_{12}\theta\frac{4\mu^2h^2}{\pi^3}\sum_{n=1,3,5,\ldots}^{\infty}\frac{1}{n^3}(-1)^{\frac{n-1}{2}}\left[1-\frac{\cosh\left(\frac{n\pi z}{\mu h}\right)}{\cosh\left(\frac{n\pi b}{2\mu h}\right)}\right]\cos\left(\frac{n\pi y}{h}\right), \tag{15}$$

where

$$\mu = \left(\frac{G_{13}}{G_{12}}\right)^{1/2}. \tag{16}$$

With the aid of Fig. 5a one can easily see that the twisting moment at one arm of the specimen is provided by the resultant of the reaction force, R_1 at roller A and R_2 at roller B. Due to the angle of twist the reaction at roller A is in fact a distributed force with a linear variation along the Z-axis at the end of the specimen ($x=a$). The distance between the influence line of R_1 and the Y axis of the cross-section is z_R. The moment equilibrium for the origin of the Y–Z coordinate system (and the application of Eq. (1)) gives

$$P_2\frac{h}{2} - P_1\frac{h}{2} + R_1z_R + R_2\frac{b}{2} = 0 \quad \text{and} \quad R_1z_R + R_2\frac{b}{2} = P\frac{h}{2}, \tag{17}$$

where $R_1z_R+R_2b/2 = M_t$ is in fact the twisting moment load on the model of the specimen arm. Although R_1, R_2 and z_R are unknowns, their product must be equal to $Ph/2$. Due to the boundary conditions the angle of twist is zero at $x=a$ and also at $x=a-s_1$, the latter is ensured by steel rollers B (see Fig. 3). It was assumed that the forces P_1 and P_2 act in the middle of the thickness (h) of the specimen arms. Due to the angle of twist it is possible that the influence line (and so the point of action) of P_1 and P_2 moves along the Y axis. The equilibrium leads even in this case to the fact that the torsional moment load is equal to $Ph/2$. The torsional moment in the coordinate system shown in Fig. 5c for the cross-section

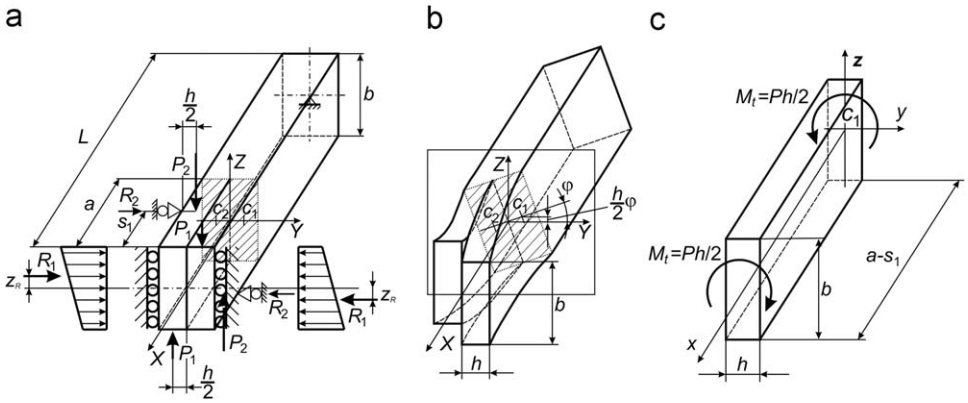

Fig. 5. The details of the beam (a), deformation of the model due to torsion (b) and the free torsion of the specimen arm (c).

with dimensions of $b\,h$ can be calculated as [28]

$$M_t = 2\int_{-b/2}^{b/2}\int_{-h/2}^{h/2}\Psi(y,z)\,dy\,dz = \frac{1}{3}G_{12}\theta\,h^3 b\varsigma. \tag{18}$$

Furthermore

$$\varsigma = 1 - \frac{192\mu}{\pi^5}\frac{h}{b}\sum_{n=1,3,5,\ldots}^{\infty}\frac{1}{n^5}\tanh\left(\frac{n\pi b}{2\mu h}\right). \tag{19}$$

A good approximation of Eq. (19) is [28]

$$\varsigma = 1 - 0.63\mu\frac{h}{b}. \tag{20}$$

Rearranging Eq. (18) we obtain

$$\theta = \frac{3M_t}{bh^3 G_{12}\varsigma}. \tag{21}$$

The angle of twist shown in Fig. 5b can be obtained by integrating θ between $0\le x\le a-s_1$. It is important to note that torsional deformation takes place only between $0\le x\le a-s_1$ because rollers A and B prevent the rotation of the cross-sections about x axis in the ranges of $a-s_1\le x\le a$, so we have

$$\varphi = \int_0^{a-s_1}\theta\,dx = \frac{3M_t(a-s_1)}{bh^3 G_{12}\varsigma}. \tag{22}$$

The angle of twist causes a displacement increment with respect to the original center of the cross-section (see Fig. 5b), which is

$$\delta_{FT} = \frac{h}{2}\varphi = \frac{3}{2}\frac{M_t(a-s_1)}{bh^2 G_{12}\varsigma} = \frac{3}{4}\frac{P(a-s_1)}{bhG_{12}\varsigma}. \tag{23}$$

3.4. Superposition of the results

The compliances at the points of load application (at rollers A and B) may be obtained by summing the results above, i.e. adding Eqs. (2), (4), (11) and (23), and Eqs. (3), (5), (12) and (23):

$$\begin{aligned} C_1 &= \frac{\delta_1}{P_1} = \frac{1}{P}\frac{s_1}{s_2}(\delta_{1EB} + \delta_{1TIM} + \delta_{1S-V} + \delta_{FT}) \\ &= \frac{s_1}{s_2}\left[\frac{2(2a^3 + (s_1+s_2)(s_1^2 - 3a^2))}{b^3 hE_{11}}\right. \\ &\quad \left. + \frac{a - s_1 - s_2}{bhkG_{13}} + \frac{6(a-s_1-s_2)a}{b^2 hE_{11}\pi}\left(\frac{E_{11}}{G_{13}}\right)^{1/2} + \frac{3}{4}\frac{a-s_1}{bhG_{12}\varsigma}\right], \end{aligned} \tag{24}$$

$$\begin{aligned} C_2 &= \frac{\delta_2}{P_2} = \frac{1}{P}\frac{s_1}{s_1+s_2}(\delta_{2EB} + \delta_{2TIM} + \delta_{2S-V} + \delta_{FT}) \\ &= \frac{s_1}{s_1+s_2}\left[\frac{2(6as_1(s_1+s_2) - s_1^2(2s_1+3s_2) - a^2(6s_1+3s_2-2a))}{b^3 hE_{11}}\right. \\ &\quad \left. + \frac{(a-s_1)}{2bhkG_{13}} + \frac{3(a-s_1-s_2)(a-s_1)}{b^2 hE_{11}\pi}\left(\frac{E_{11}}{G_{13}}\right)^{1/2} + \frac{3}{8}\frac{a-s_1}{bhG_{12}\varsigma}\right]. \end{aligned} \tag{25}$$

The total compliance (at roller C) can be computed based on Fig. 3 by applying a linear interpolation. From Fig. 3 it follows that

$$\frac{\delta}{2} = \delta_2\frac{s_1+s_2}{s_1} - \delta_1\frac{s_2}{s_1}. \tag{26}$$

On the other hand we can use the following relationships:

$$C_1 = \frac{\delta_1}{P_1} \Rightarrow \delta_1 = C_1 P_1, C_2 = \frac{\delta_2}{P_2} \Rightarrow \delta_2 = C_2 P_2. \tag{27}$$

Substituting Eq. (27) into Eq. (26) leads to the following:

$$\frac{\delta}{2} = C_2 P\left(\frac{s_1+s_2}{s_1}\right)^2 - C_1 P\left(\frac{s_2}{s_1}\right)^2. \tag{28}$$

Dividing Eq. (28) with the applied load, P we have

$$\frac{C}{2} = C_2\left(\frac{s_1+s_2}{s_1}\right)^2 - C_1\left(\frac{s_2}{s_1}\right)^2, \tag{29}$$

where C is the compliance of the system at roller C. The combination of Eqs. (24) and (25) with Eq. (29) gives

$$\begin{aligned} \frac{C}{2} &= \frac{4(a^3 + 3(s_1+s_2)a^2 + 3(s_1+s_2)^2 a - (2s_1 s_2^2 + 3s_1^2 s_2 + s_1^3)}{b^3 hE_{11}} \\ &\quad + \frac{as_1 + s_2^2 - s_1^2}{bhkG_{13}s_1} + \frac{6(a-(s_1+s_2))^2}{b^2 hE_{11}\pi}\left(\frac{E_{11}}{G_{13}}\right)^{1/2} + \frac{3}{4}\frac{a-s_1}{bhG_{12}\varsigma}. \end{aligned} \tag{30}$$

Taking this compliance two times (due to the two arms of the specimen) and rearranging the result we have

$$\begin{aligned} C &= \frac{8a^3}{b^3 hE_{11}}\left[1 - 3\left(\frac{s_1+s_2}{a}\right) + 3\left(\frac{s_1+s_2}{a}\right)^2 - \frac{s_1(s_1+s_2)(s_1+2s_2)}{a^3}\right] \\ &\quad + \frac{8a^3}{b^3 hE_{11}}\left[0.3\left(1 - \frac{s_2^2 - s_1^2}{as_1}\right)\left(\frac{b}{a}\right)^2\left(\frac{E_{11}}{G_{13}}\right) + 0.19\frac{1}{\varsigma}\left(1 - \frac{s_1}{a}\right)\left(\frac{b}{a}\right)^2\left(\frac{E_{11}}{G_{12}}\right)\right] \\ &\quad + \frac{8a^3}{b^3 hE_{11}}\left[0.48\left(\frac{a-(s_1+s_2)}{a}\right)^2\left(\frac{b}{a}\right)\left(\frac{E_{11}}{G_{13}}\right)^{1/2}\right]. \end{aligned} \tag{31}$$

Or in a more convenient form:

$$C = \frac{8a^3}{b^3 hE_{11}}[f_{EB1} + f_{TIM1} + f_{FT1} + f_{S-V1}], \tag{32}$$

where

$$f_{EB1} = 1 - 3\left(\frac{s_1+s_2}{a}\right) + 3\left(\frac{s_1+s_2}{a}\right)^2 - \frac{s_1(s_1+s_2)(s_1+2s_2)}{a^3}, \tag{33}$$

$$f_{TIM1} = 0.3\left(1 - \frac{s_2^2 - s_1^2}{as_1}\right)\left(\frac{b}{a}\right)^2\left(\frac{E_{11}}{G_{13}}\right), \tag{34}$$

$$f_{FT1} = 0.19\frac{1}{\varsigma}\left(1 - \frac{s_1}{a}\right)\left(\frac{b}{a}\right)^2\left(\frac{E_{11}}{G_{12}}\right), \tag{35}$$

$$f_{S-V1} = 0.48\left(\frac{a-(s_1+s_2)}{a}\right)^2\left(\frac{b}{a}\right)\left(\frac{E_{11}}{G_{13}}\right)^{1/2}. \tag{36}$$

The energy release rate may be obtained using the Irwin–Kies expression [30]

$$G_C = \frac{P^2}{2b}\frac{dC}{da}, \tag{37}$$

which results in

$$\begin{aligned} G_{MSCB} &= \frac{12P^2a^2}{b^4hE_{11}}\left[1 - 2\left(\frac{s_1+s_2}{a}\right) + \left(\frac{s_1+s_2}{a}\right)^2\right] \\ &\quad + \frac{12P^2a^2}{b^4hE_{11}}\left[0.1\left(\frac{b}{a}\right)^2\left(\frac{E_{11}}{G_{13}}\right) + 0.06\frac{1}{\varsigma}\left(\frac{b}{a}\right)^2\left(\frac{E_{11}}{G_{12}}\right)\right] \\ &\quad + \frac{12P^2a^2}{b^4hE_{11}}\left[0.32\left(1 - \frac{s_1+s_2}{a}\right)\right]\left(\frac{b}{a}\right)\left(\frac{E_{11}}{G_{13}}\right)^{1/2}. \end{aligned} \tag{38}$$

Rearranging Eq. (38) we have

$$G_{MSCB} = \frac{12P^2a^2}{b^4hE_{11}}[f_{EB2} + f_{TIM2} + f_{FT2} + f_{S-V2}], \tag{39}$$

where

$$f_{EB2} = 1 - 2\left(\frac{s_1+s_2}{a}\right) + \left(\frac{s_1+s_2}{a}\right)^2, \tag{40}$$

Table 1
Contribution of the various theories and effects to the total compliance and ERR in the MSCB specimen if $P = 200$ N and $s_1 = 41$ mm and $s_2 = 49$ mm.

a (mm)	80	85	90	95	100	105	110	120	130	140	150	160
C_{EB}	23.07	23.16	23.18	23.19	23.28	23.54	24.04	26.08	30.04	36.58	46.35	59.98
C_{TIM}	2.797	2.940	3.084	3.227	3.370	3.514	3.657	3.944	4.231	4.517	4.804	5.091
C_{SV}	0.153	0.038	0.000	0.038	0.152	0.343	0.611	1.376	2.446	3.822	5.504	7.491
C_{FT}	0.892	1.007	1.121	1.236	1.350	1.464	1.579	1.808	2.037	2.265	2.495	2.723
G_{EB}	71.51	17.88	0.000	17.88	71.51	160.9	286.0	643.6	1144.2	1787.9	2574.5	3504.2
G_{TIM}	63.72	63.72	63.72	63.72	63.72	63.72	63.72	63.72	63.72	63.72	63.72	63.72
G_{SV}	−67.95	−33.97	0.000	50.86	67.95	101.9	135.9	203.8	271.8	339.7	407.7	475.64
G_{FT}	50.86	50.86	50.86	50.86	50.86	50.86	50.86	50.86	50.86	50.86	50.86	50.86

Compliances: $(\text{mm/N}) \times 10^{-3}$ C_{EB} – Euler-Bernoulli beam theory, C_{TIM} – Timoshenko beam theory, C_{SV} – Saint-Venant effect. C_{FT} – free torsion effect,
ERRs: (J/m^2) G_{EB} – Euler-Bernoulli beam theory, G_{TIM} – Timoshenko beam theory, G_{SV} – Saint-Venant effect. G_{FT} – free torsion effect.

$$f_{TIM2} = 0.1\left(\frac{b}{a}\right)^2\left(\frac{E_{11}}{G_{13}}\right), \tag{41}$$

$$f_{FT2} = 0.06\frac{1}{\varsigma}\left(\frac{b}{a}\right)^2\left(\frac{E_{11}}{G_{12}}\right), \tag{42}$$

$$f_{S-V2} = 0.32\left(1-\frac{s_1+s_2}{a}\right)]\left(\frac{b}{a}\right)\left(\frac{E_{11}}{G_{13}}\right)^{1/2} \tag{43}$$

If $a = s_1{+}s_2$ then $f_{EB2} = 0$ (Eq. (40)) and $f_{S-V2} = 0$ (Eq. (43)), i.e. the ERRs by bending and Saint-Venant effect become zero. If we substitute $s_1 = s_2 = s$ into Eqs. (32)–(36) and Eqs. (39)–(43) then we obtain the analytical expressions given in [27].

3.5. Contributions to C and to ERR

Table 1 demonstrates the contribution of the various deformations to the total compliance and ERR in the crack length range of $a = 85$–160 mm. The applied material properties are $E_{11} = 33$ GPa, $G_{12} = G_{13} = 3$ GPa, while the geometrical parameters are $b = 9$ mm, $2h = 6.2$ mm, $s_1 = 41$ mm, $s_2 = 49$ mm. The models were loaded by an applied load of $P = 200$ N, which was chosen arbitrarily.

For both the C and ERR the most dominant term is from bending. The shear deformation and free torsion terms depend linearly on the crack length, while the Saint-Venant effect is proportional to the square of a.

The ERR by bending becomes zero if $a = 90$ mm ($a = s_1{+}s_2$); on the contrary, in greater crack lengths the bending is the most dominant term. It is also important that the Saint-Venant effect gives negative ERR if $a = 80$ and 85 mm. This indicates that in this range the Saint-Venant effect acts against the other three effects. The contribution of transverse shear and free torsion to the ERR is a constant term, which is a significant fraction mainly at lower cracks. Overall, the four mechanical effects are equally important to be considered in an accurate analytical model.

4. Finite element analysis

The finite element analysis was performed using the COSMOS/M 2.6 package. The models were built using linear eight-node SOLID brick elements. The finite element model is shown in Fig. 6 including the magnified crack tip zone. Similar models were used for example in [31]. The elastic properties of the models are $E_{11} = 33$ GPa, $E_{22} = E_{33} = 7.2$ GPa, $G_{12} = G_{13} = G_{23} = 3$ GPa and $\nu_{12} = \nu_{13} = \nu_{23} = 0.27$. The boundary conditions for the finite element model were the same as those shown in Fig. 5a. The geometrical properties are $b = 9$ mm, $2h = 6.2$ mm, and the length of the models is $L = 160$ mm (refer to Fig. 4). The models consisted of 18,624 elements, while the number of nodes – depending on the area of the crack faces – was about 23,000. The penetration of the nodes in the crack faces was eliminated by imposing the same displacements in the y direction by using the command CPDOF. The CPDOF command enables such restrictions only for 500 pairs of node. Since in greater crack lengths the number of node pairs was more than 500, only the nodes at the specimen sides (at $y = \pm b/2$) were constrained. At the crack front mode-II and mode-III ERRs were evaluated using the virtual crack-closure technique (VCCT) [32]; the size of the crack tip elements was $\Delta x = \Delta y = 0.25$ mm and $\Delta z = 0.75$ mm (refer to Fig. 6 for the coordinate system). The elements of the model were checked and no errors or warnings were received. In each case the mode-I ERR component was zero along the crack front. The reasons for the FE analysis were to

- confirm the applicability and accuracy of the analytical solution
- demonstrate the distribution of mode-II and mode-III ERRs along the crack front and
- give some guidelines in order to choose the optimal geometrical parameters of the MSCB specimen for a nearly pure mode-III test.

4.1. The optimal geometrical parameters

In [3] it has been mentioned that if $a = s_1{+}s_2$ then the bending moment at the crack front is zero, i.e. mode-II contribution is reduced. In the end of Section 3.5 it was confirmed, since $f_{EB2} = 0$ and $f_{SV2} = 0$. In order to choose the ratio of the crack length and s_1, s_2 consider now Table 2, wherein the ERRs were evaluated in the crack length range of $a = 85$–160 mm. Mode-II and mode-III ERR distributions were integrated and the width-wise average values were determined using the ORIGINPRO 7.0 package. Since there is a large number of works that show similar distributions [3,4,15,16,22], the diagrams are not shown here. In Table 2 the width-wise average mode-II and mode-III contributions to the total ERR, the difference between the beam and FE model (considering again the width-wise average value of G_{III}) and the ratio of G_{III}/G_{II} at the ends of the crack front ($z = \pm b/2$, refer to Fig. 5) are given. The latter is important in order to ensure that at the specimen sides, where the crack growth may be followed also in non-transparent materials, the fracture is mode-III dominated. In accordance with Table 2 the mode-II component is less if $a = 95$ mm, while the difference between the beam and FE models is the smallest if $a = 98$ mm. However, in the latter case mode-III dominance is about 1 at the specimen sides. The reasonable crack length range is $a = 92$–98 mm, i.e. based on the finite element analysis the recommended $a/(s_1{+}s_2)$ ratio for the MSCB configuration is

$$1.02 \le a/(s_1+s_2) \le 1.09. \tag{44}$$

Table 2
Effect of crack length on the mode-II and mode-III ERRs and comparison with the beam model.

a (mm)	85	90	92	94	95	96	97	98	100	105
$G_{II,FEM}/(G_{II,FEM}+G_{III,FEM})$	35.49	8.50	3.50	1.62	1.45	1.82	2.49	3.48	6.04	13.59
$G_{III,FEM}/(G_{II,FEM}+G_{III,FEM})$	64.51	91.50	96.50	98.38	98.55	98.18	97.51	96.52	93.96	86.41
$(G_{III,FEM}-G_{Beam})/G_{Beam}$	−24.14	4.45	7.37	6.62	5.22	3.58	1.61	−0.53	−5.03	−15.77
$(G_{III,FEM}/G_{II,FEM})_{x=\pm b/2}$	1.23	143.23	9.38	3.10	2.19	1.66	1.32	1.09	0.80	0.47

$G_{II,FEM}$, $G_{III,FEM}$ – ERRs from FE analyis, G_{Beam} – ERR from beam analyis.

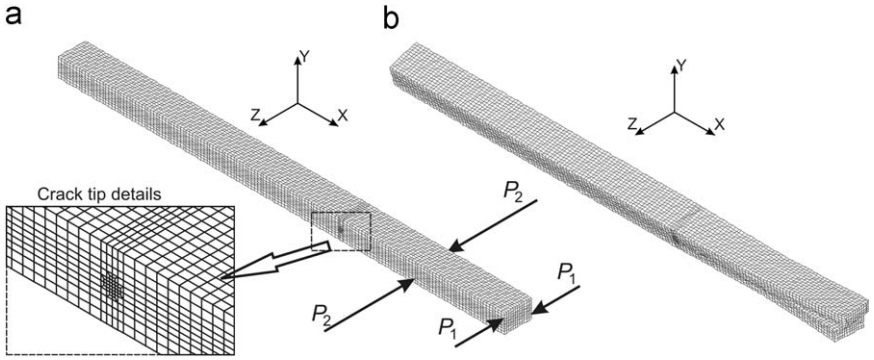

Fig. 6. The finite element model (a) and the deformed shape (b) of the MSCB specimen.

Based on the analysis performed it is obvious that the width-wise average values of the ERR change with crack length; hence during crack propagation the mode ratio also changes. This indicates that the MSCB specimen should be used essentially for crack initiation measurements.

Fig. 7 shows the distribution of the mode-I, mode-II and mode-III ERRs along the crack front if $s_1 = 41$, $s_2 = 49$ mm, $a = 95$ mm and $P = 175$ N. It is seen that the fracture is pure mode-III dominated at the center of the specimen, while at the ends of the crack front the value of mode-III ERR is sufficiently higher than that of mode-II.

4.2. Comparison with the analytical model

Fig. 8a shows the compliance values at both rollers, A and B, of one of the specimen arms, as well as the total compliance (C) of the MSCB specimen (Eq. (32)). Fig. 8a shows that the analytical model is very accurate compared to the FE results. Cicci et al. [33] performed a similar beam analysis; however, their model was not in much good agreement with the FE results as the present one. The reason for that is they accounted only for bending and shear. Fig. 8b demonstrates the ratio of the FE and beam theory solutions. The difference between the numerical and analytical solutions for C_1 goes to $\pm$infinity, which can be explained by Fig. 8a, showing that C_1 changes its sign at $a = 124.24$ mm. Finally in Fig. 8c the angles of twist are displayed at the specimen end and at the delamination front by the FE model together with the analytical prediction at $x = 0$ (refer to Fig. 5b). In each case the load is $P = 200$ N. Although the difference increases with crack length, the agreement is excellent. Finally, referring to Fig. 7, we can see that the width-wise average of mode-III ERR is 134.1 J/m^2 against the result of the beam model, which is 127.4 J/m^2 (note that $P = 175$ N was applied). This is a 5% difference. All of these results confirm the applicability of the analytical model.

In the following the performed experimental work is detailed including the fabrication of the specimens, the details of the experimental work, the reduction of the measured data and finally the application of the developed beam model.

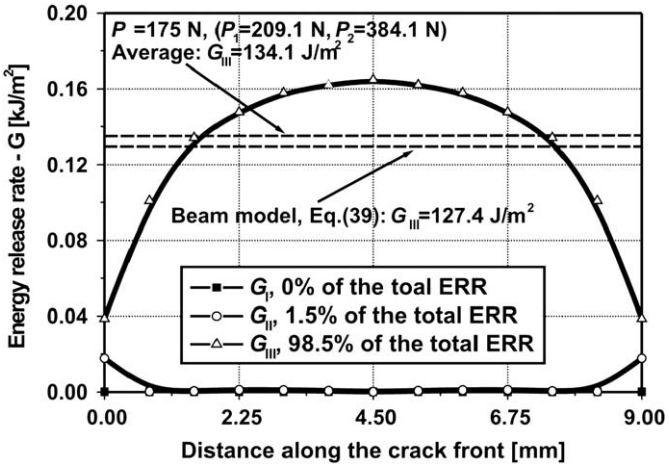

Fig. 7. The distribution of the mode-I, mode-II and mode-III energy release rates along the crack front in the MSCB specimen.

5. Experiments

The constituent materials of the E-glass/polyester composite material applied in the present study were procured from Novia Ltd. The properties of the E-glass fiber are $E = 70$ GPa and $\nu = 0.27$, while for the unsaturated polyester resin we have $E = 3.5$ GPa and $\nu = 0.35$. Both were considered to be isotropic. The unidirectional ($[0^\circ]_{14}$) E-glass/polyester specimens with thickness of $2h = 6.2 \pm 0.05$ mm, width of $b = 9 \pm 0.05$ mm, and fiber-volume fraction of $V_f = 43\%$ were manufactured in a special pressure tool. A polyamide (PA) insert with thickness of 0.03 mm was placed at the midplane of the specimens to make an artificial starting defect. A great advantage of the present E-glass/polyester material is the transparency, which makes it possible to observe visually the crack initiation/propagation. The tool was left at room temperature until the specimens became dry. Then the specimens were removed from the tool and were further left at room temperature until 4–6 h. The specimens were cut to the desired

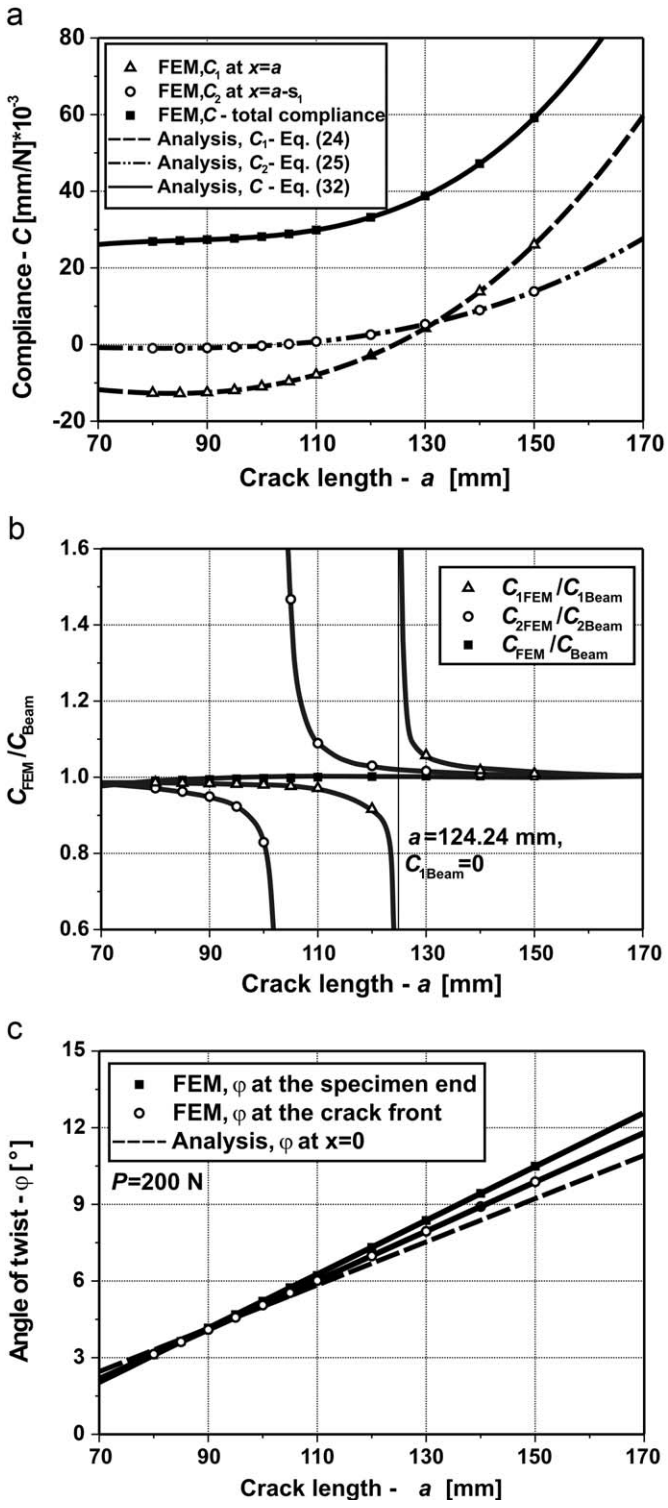

Fig. 8. Comparison of the compliances by finite element method and beam theory (a), the ratio of the numerical and analytical compliances (b) and comparison of the angles of twist by finite element and beam analysis (c).

length and were precracked in opening mode of 4–5 mm using a sharp blade. The reason for that was in this case it was possible to make a straight crack front, which is important in the case of the crack length measurement and the observation of the crack initiation.

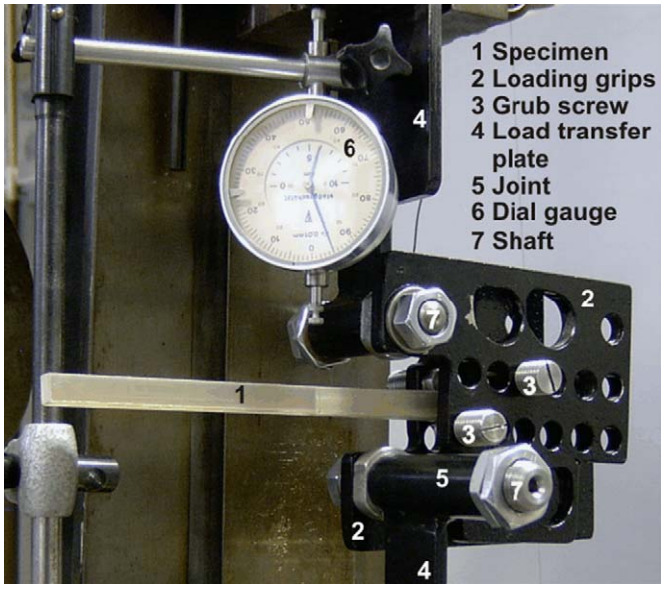

Fig. 9. The experimental equipment for the mode-III modified split-cantilever beam (MSCB) specimen.

5.1. Material properties

The flexural modulus of the tested specimens was determined from a three-point bending test with a span length of $2L = 150$ mm using six uncracked specimens with $2h = 6.2$ mm and $b = 20$ mm. The flexural modulus was calculated based on the slope of the measured load–displacement curves using a simple beam theory expression. Then the specimens were cut along the longitudinal direction in order to obtain very narrow specimens. The narrow specimens were rotated by 90° about the longitudinal axis compared to the original measurements and the slope of the load–displacement curve was calculated, the modulus of the specimens was determined from a simple beam theory expression again. Both experiment resulted in $E_{11} = 33$ GPa, i.e. the material was found to be transversely isotropic. The additional properties were predicted using simple rule of mixture; in this way $E_{22} = E_{33} = 7.2$ GPa, $G_{12} = G_{13} = 3$ GPa and $\nu_{12} = \nu_{13} = \nu_{23} = 0.27$ were obtained. The material properties were used only in the data reduction process. It should be mentioned that the G_{13} has a significant influence on both the compliance and ERR and it is assumed that for unidirectional composites the traditional rule of mixture is sufficiently accurate [34].

5.2. Data recording and reduction

For the measurements 11×4 specimens were used (4 specimens were used in each crack length) with $2h = 6.2$ mm, $b = 9$ mm and with the following crack lengths: $a = 80$, 85, 90, 95, 100, 105, 110, 120, 130, 140 and 150 mm. Each specimen was put into the loading rig as shown in Fig. 9; the rig was adjusted in order to eliminate any play of the specimens. Then the specimens were loaded subsequently, the load and displacement values were read from the scale of the testing machine and using the mechanical dial gauge. The crack initiation was identified visually, so when the first non-uniformity concerning the straight crack front was observed it was believed to be the point of crack initiation.

Although previous works reported very low compliance (defined as δ/P) values for the MSCB configuration using high modulus composite material [3,7,33], it may be assumed that for the present glass/polyester composite with a relatively low flexural modulus and due to the significant modification of the

original rig it may be applied. The load–displacement curves were fit with a linear function including the measured points until crack initiation and the compliance at each crack length was determined from the slope of the P–δ curves. Then the compliance values were fit with a third-order polynomial of the form

$$C = C_0 + C_1 a + C_2 a^2 + C_3 a^3, \tag{45}$$

where the coefficients C_i, $i = 0 \ldots 3$ were determined by least square fitting, while ERR was determined with the help of Eq. (37). A significant advantage of this method is that there is no need to determine the elastic properties of the material.

In accordance with direct beam theory (DBT) it is possible to obtain very simple reduction schemes for DCB and ENF systems, see e.g. [35]. The combination of Eqs. (32), (37) and (39) results in

$$G_{DBT} = \frac{3P\delta}{2ba}\left(\frac{f_{EB2} + f_{TIM2} + f_{FT2} + f_{S-V2}}{f_{EB1} + f_{TIM1} + f_{FT1} + f_{S-V1}}\right), \tag{46}$$

where the coefficients in the parentheses are given by Eqs. (33)–(36) and Eqs. (40)–(43). In Eq. (46) P and δ are the experimentally measured load and displacement values at the point of crack initiation. The first term in Eq. (46) is the same as the DBT scheme for the DCB specimen [35].

6. Results and discussion

6.1. Load–displacement and compliance

Fig. 10a demonstrates some of the measured load–displacement curves up to fracture initiation including several crack lengths. The load–displacement curves show a typical linear behaviour justifying the application of linear elastic fracture mechanics (LEFM). Fig. 10b shows how the load required for crack initiation decreases as the function of crack length. The scatter of the data is also shown, indicating reasonable ranges. Overall, based on Figs. 10a and b the MSCB specimen shows very similar behaviour compared to the results of experiments performed on double-cantilever beam (DCB) and mode-II end-loaded split (ELS) systems for the same material [35,36].

The measured compliance values are shown in Fig. 11. The hollow circles show the experimentally measured points together with the scatter of the data (at each point four specimens were measured); the fit curve is plotted with dashed black line. The scatter is within reasonable ranges and proves the accuracy of the system. It should be emphasized that it required very accurate measurements and the points were determined from the slope of the P–δ curves. At each crack length four specimens were tested, the compliances at each crack length in Fig. 11 was the averaged slope of the four load–displacement curves. The compliance curve is very similar to results obtained for mode-I and mode-II specimens for the same material [36,37]. In fact the analytical curve is presented with a continuous line, indicating very good agreement with the experimentally measured points. The results in Fig. 11 show the accuracy of both the experimental equipment presented in Fig. 2 and the analytical model.

It should be kept in mind that in the work by Cicci et al. [33] the friction between crack faces (which is induced by the waviness of the crack plane) was assumed to be one of the reasons for the poor agreement between analysis and experiment, respectively, and for the large scatter of the experimentally measured compliance values. In spite of that, for the present E-glass/polyester composite material the experimental results showed a good correlation to the analytical compliance curve. Based on the present measurements and the compliance curves presented in Fig. 11 it may be assumed that the effect of friction

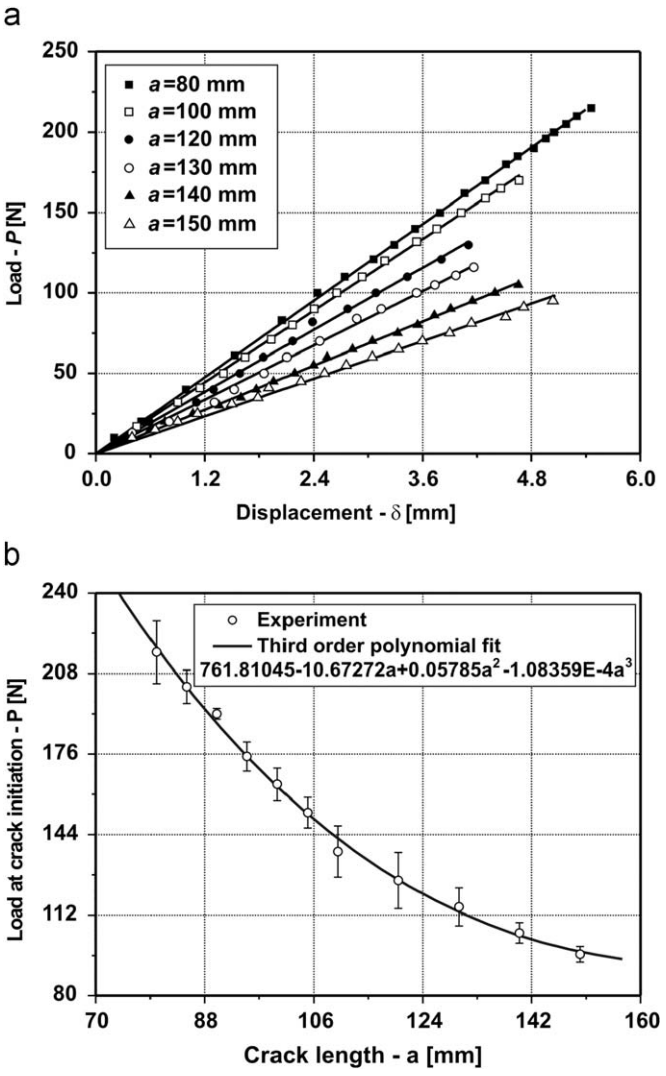

Fig. 10. Load–displacement curves up to fracture initiation (a) and the load at initiation versus the crack length (b).

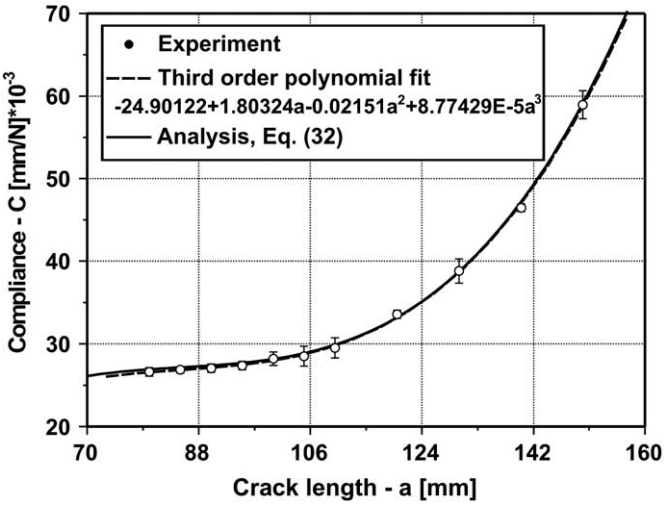

Fig. 11. The measured compliance values and comparison of the analytical and fit curves.

on the compliance of the MSCB specimen is negligible. Moreover the differences between the experimental and analytical compliances experienced by Cicci et al. rather can be related to Saint-Venant and free torsion effects, which were not considered in their work.

Considering the possible frictional effects it may be assumed that the twisting of the specimen arms partly or entirely eliminates the frictional effect. On the other hand the steel rollers – which ensures zero crack opening – cause also friction between the crack faces. However, in this case the compressive force, which is transferred to the rollers by the specimen ends shown in Fig. 5, is estimated to be insignificant. The frictional surfaces are relatively small, especially compared to the ECT specimen. Zhao and Wang [14] applied ECT specimens with dimension of $38.1 \times 88.9\,mm^2$ (width × length) and with crack lengths within 13.46–19.305 mm. So, the possible frictional surface is equal to $1196.6–1716.3\,mm^2$. For comparison the possible frictional surface in the MSCB specimen is $a \cdot b = 95 \cdot 9 = 855\,mm^2$, which is in the same order; however, in the ECT specimen the normal force is actually the external load (which increases until crack initiation), while in the MSCB specimen the external load is independent of the normal force. Furthermore, the normal force in the MSCB specimen can be reduced to almost zero by properly adjusting the sideways (y) position of the loading plates (see the number of "3" in Fig. 2). It is also important to highlight that the contact force between the steel rollers (see Fig. 3) and specimen arms try to open the crack and they act against the frictional effect.

6.2. Energy release rate

Table 3 lists the ERRs calculated by the CC method, the improved beam theory (IBT) and DBT. An immediate observation is that the difference between the IBT and the CC method is significant; the best agreement is reached if $a = 120$ mm. The highest difference between the ERR by the CC method and IBT is 18.9% at $a = 90$ mm. The DBT method produces very similar results to those by the IBT method, which is not surprising, since the factors in Eq. (46) are based on the beam analysis. It is important to note that a relatively high mode-III dominant condition exist only at $a = 90–100$ mm; the ERRs at the other crack lengths are listed only for comparison purposes.

It is shown in Fig. 11 that the analytical and fit curves show a very good agreement, although the derivative of the fit curve is very sensitive even to the smallest change in the measured compliance values. So it seems that the application of the CC method is still uncertain and it is a reasonable assumption that the IBT or DBT provides higher accuracy, and so the derivative of the analytical $C(a)$ curve and also the ERR will be also more accurate if we use Eqs. (32) and (39).

Based on the work performed the recommended data reduction scheme for the MSCB system is IBT or DBT. It seems that the efficiency of the CC cannot be improved due to the insignificant changes of the compliance in the region, where the test produces mode-III dominated fracture (see Table 1).

Finally, referring to some previous work we give a comparison of the ERRs under the three pure fracture mode conditions. The ERR is $G_{IIIC} = 127.4\,J/m^2$ ($a = 95$ mm) from the IBT method (98.2% mode-III). For comparison for the same material using 20 mm wide specimens, mode-I and mode-II ERR at the same crack length ($a = 95$ mm) were $G_{IC} = 396.7\,J/m^2$, $G_{IIC} = 813.11\,J/m^2$ [36,37]. Both were calculated using the IBT.

So if $a = 95$ mm, G_{III} is significantly lower than G_I and G_{II} in the present glass/polyester material. In a recent paper [27] the mode-III ERR was determined to be $G_{III} = 445.7\,J/m^2$ at $a = 55$ mm for the same material. Although the experimental equipment was significantly modified since then, the results show that G_{III} decreases with crack length.

6.3. The role of the MSCB specimen

The MSCB specimen is the only mode-III configuration, which is suitable to investigate the effect of crack length on the critical ERR at crack initiation in an extended crack length range. The only requirement to produce the mode-III dominant fracture is Eq. (44). Applying different s_1 and s_2 values a quite extended crack length range can be covered, e.g., in our equipment the range of $a = 42–98$ mm can be investigated. Studies employing the ECT and ACPB systems confirm the significant dependence of G_{III} on the crack length. However, while the ECT tests show increasing ERR with the crack length [15,16]; using the APCB method, Farshad and Flüeler [17] experienced decreasing stress intensity factors with the crack length. Although this is a contradiction, there are some major questions that should be clarified.

Both the ECT and APCB specimens apply limited crack length ranges. In the paper by Liao [13] the crack length was varied between 7.8 and 14.3 mm; Li et al. [11] applied specimens with $a = 7.6–22.9$ mm. Farshad and Flüeler investigated the APCB specimens with $a = 1–9$ mm. In some recent studies, Ratcliffe [15] and Pennas and Cantwell [16] studied ECT specimens with dimensions of $38 \times 108\,mm^2$ and investigated the $a = 19–26.6$ mm range. In each of these studies the crack length range is less than 16 mm. To confirm the dependence of mode-III ERR on crack length, it is desired to use a more extended range. Finally, each paper presents comparison with results of mode-I and mode-II tests, leading to the conclusion that mode-III ERR is significantly higher than mode-I and mode-II toughnesses. It would be reasonable to compare the ERRs under different fracture modes at the crack length, when the ERR becomes independent of a. It is also important to note that the MSCB maintains the traditional specimen geometry and could be more convenient for comparison purposes with results obtained using DCB and ENF tests. A study including the effect of crack length and specimen width on mode-III ERR will be presented in the future including an extended crack length range using the MSCB specimen.

Table 3
Values of the ERR against the crack length by compliance calibration method, improved beam theory and direct beam theory.

A (mm)	80	85	90	95	100	105	110	120	130	140	150
G_C[a]	120.9 ± 13.8	110.5 ± 7.2	130.2 ± 2.9	156.6 ± 10.3	199.7 ± 15.3	244.3 ± 19.4	269.1 ± 40.3	381.1 ± 68.6	488.0 ± 65.2	576.2 ± 44.8	659.0 ± 43.0
G_{Beam}[b]	138.8 ± 19.6	101.3 ± 6.7	105.6 ± 2.8	127.5 ± 8.4	171.0 ± 10.5	220.4 ± 16.8	253.7 ± 38.8	382.6 ± 86.5	509.9 ± 68.2	618.7 ± 33.6	721.5 ± 43.8
G_{DBT}[c]	137.5 ± 18.2	100.2 ± 6.6	104.4 ± 2.9	126.1 ± 8.2	171.2 ± 10.2	218.4 ± 24.8	250.7 ± 37.1	387.7 ± 75.5	510.8 ± 66.9	609.3 ± 51.7	719.2 ± 42.5
diff[ab] (%)	−14.8	8.4	18.9	18.6	14.4	9.8	5.7	−0.4	−4.5	−7.4	−9.5
diff[ac] (%)	−13.7	9.4	19.9	19.5	14.3	10.6	6.8	−1.7	−4.7	−5.7	−9.1

G_C[a] – ERR by compliance calibration method (J/m^2).
G_{Beam}[b] – ERR by beam theory (J/m^2).
G_{DBT}[c] – ERR by direct beam theory (J/m^2).

7. Conclusions

In this work the modified split-cantilever beam specimen was revisited, updated and found to be a promising candidate for the measurement of the mode-III interlaminar fracture toughness of composites. An improved analytical solution was developed for the specimen, which accounts for four different mechanical deformations: bending, transverse shear, Saint-Venant effect and the free torsion of the specimen arms. Analyzing these effects the compliance and the energy release rate of the specimen were determined and were compared to finite element results. The comparison showed a very good agreement. Considering the compliance values calculated by the analytical and finite element solution the difference is absolutely negligible, while in the case of the energy release rate the difference between the virtual crack-closure technique and the analysis depends on the crack length. For this reason some recommendations for the choice of the geometrical parameters were made in order to obtain a test, which provides a 98% mode-III interlaminar fracture. In the optimal case the difference between the analytical and finite element model is about 5%.

In order to confirm the application of the analytical model, experiments were also performed. A modified experimental equipment was presented, which included accurate and careful design. The measured data were reduced using the compliance calibration technique, direct beam theory and the analytical model.

The experimentally and analytically calculated compliances agreed excellently. In spite of that at some crack lengths the energy release rate calculated by the CC method and IBT showed large differences (18.6% in the worst case). The main reason for that is evidently that the compliance of the specimen is almost independent on the crack length in the crack length range where mode-III dominance is produced. Therefore, the compliance calibration method is not recommended for data reduction, and the improved beam theory seems to be the optimal reduction tool. Alternatively, the direct beam theory gives approximately the same results for the ERRs as IBT, but it incorporates also the experimentally measured displacement at the point of crack initiation.

Despite nowadays most of the works proposing the edge-crack torsion test for mode-III, there are some major questions that could be addressed only by the modified split-cantilever beam. For example the MSCB specimen provides a larger available crack length range to reveal the dependence of mode-III ERR on crack length. On the other hand the MSCB maintains the traditional beam-like specimen geometry (same as those of the DCB and ENF specimens), and consequently it is more convenient for comparison purposes.

Acknowledgements

This paper was supported by the János Bolyai Research Scholarship of the Hungarian Academy of Sciences and the National Science and Research Fund (OTKA) under Grant no. T34040. The author is grateful to Professor Mark T. Kortschot (University of Toronto) for providing [3,7,32]. I am also grateful to my father, András L. Szekrényes, for the manufacturing of the experimental equipments.

References

[1] Becht G, Gillespie Jr JW. Design and analysis of the crack rail shear specimen for mode III interlaminar fracture. Composites Science and Technology 1988;31:143–57.
[2] Donaldson SL. Mode III intelaminar fracture characterization of composite materials. Composites Science and Technology 1988;32:225–49.
[3] Sharif F, Kortschot MT, Martin RH. Mode III delamination using a split cantilever beam. In: Martin RH, editor. Composite materials: fatigue and fracture ,Fifth Volume ASTM STP 1230. ASTM: Philadelphia; 1995. p. 85–99.
[4] Hwang S-F, Hu C-L. Tearing mode interlaminar fracture toughness of composite materials. Polymer Composites 2001;22:57–64.
[5] Naik NK, Reddy KS, Meduri S, Raju NB, Prasad PD, Azad SKNM, Ogde PA, Reddy BCK. Interlaminar fracture characterization for plain weave fabric composites. Journal of Materials Science 2002;37:2983–7.
[6] Robinson P, Sonq QD. The development of an improved mode III delamination test for composites. Composites Science and Technology 1994;52:217–33.
[7] Trakas K, Kortschot MT. The relationship between critical strain energy release rate and fracture mode in multidirectional carbon-fiber/epoxy laminates. In: Armanios EA, editor. Composite Materials: Fatigue and Fracture – Sixth Volume ASTM STP 1285ASTM; 1997. p. 283–304.
[8] Rizov V, Shindo Y, Horiguchi K, Narita F. Mode III interlaminar fracture behaviour of glass fiber reinforced polymer woven laminates at 293 to 4 K. Applied Composite Materials 2006;13:287–304.
[9] Lee SM. An edge crack torsion method for mode III delamination fracture testing. Journal of Composites Technology and Research 1993;15(3):193–201.
[10] Adams DF, Carlsson LA, Pipes RB. Experimental characterization of advanced composite materials, third edition. Boca Raton, London, New York, Washington: CRC Press; 2003.
[11] Li X, Carlsson LA, Davies P. Influence of fiber volume fraction on mode III interlaminar fracture toughness of glass/epoxy composites. Composites Science and Technology 2004;64:1279–86.
[12] Suemasu H. An experimental method to measure the mode-III interlaminar fracture toughness of composite materials". Composites Science and Technology 1999;59:1015–21.
[13] Liao WC, Sun CT. The determination of mode III fracture toughness in thick composite laminates. Composites Science and Technology 1996;56:489–99.
[14] Zhao D, Wang Y. Mode III fracture behaviour of laminated composite with edge crack in torsion. Theoretical and Applied Fracture Mechanics 1998;29:109–23.
[15] Ratcliffe JG. Characterization of the edge crack torsion (ECT) test for mode III fracture toughness measurement of laminated composites. NASA/Technical Memorandum-2004-213269.
[16] Pennas D, Cantwell WJ, Compston P. The influence of strain rate on the mode III interlaminar fracture of composite materials. Journal of Composite Materials 2007;41:2595–14.
[17] Farshad M, Flüeler P. Investigation of mode III fracture toughness using an anti-clastic plate bending method. Engineering Fracture Mechanics 1998;60:5–6.
[18] Podczeck F. The determination of fracture mechanics properties of pharmaceutical materials in mode III loading using an anti-clastic plate bending method. International Journal of Pharmaceutics 2001;227:39–46.
[19] Ehart RJA, Stanzl-Tschegg SE, Tschegg EK. Crack face interaction and mixed mode fracture of wood composites during mode III loading. Engineering Fracture Mechanics 1998;61:253–78.
[20] Ehart RJA, Stanzl-Tschegg SE, Tschegg EK. Mode III fracture energy of wood composites in comparison to solid wood. Wood Science Technology 1999;33:391–405.
[21] Kostopoulos V, Markopoulos YP. On the fracture toughness of ceramic matrix composites. Material Science and Manufacturing A 1998;250:303–12.
[22] Yoshihara H. Examination of the 4-ENF test for measuring the mode III R-curve of wood. Engineering Fracture Mechanics 2006;73:42–63.
[23] Olsson R. A simplified improved beam analysis of the DCB specimen. Composites Science and Technology 1992;43:329–38.
[24] Carlsson LA, Gillespie JW, Pipes RB. On the analysis and design of the end notched flexure (ENF) specimen for mode II testing. Journal of Composite Materials 1986;20:594–604.
[25] Ozdil F, Carlsson LA, Davies P. Beam analysis of angle-ply laminate end-notched flexure specimens. Composites Science and Technology 1998;58:1929–38.
[26] Szekrényes A. Prestressed fracture specimen for delamination testing of composites. International Journal of Fracture 2006;139:213–37.
[27] Szekrényes A. Delamination fracture analysis in the G_{II}–G_{III} plane using prestressed transparent composite beams. International Journal of Solids and Structures 2007;44:3359–78.
[28] Timoshenko S, Goodier JN. Theory of elasticity. New York, Toronto, London: McGraw-Hill Book Company; 1951.
[29] Sankar BV. A beam theory for laminated composites and application to torsion problems. Journal of Applied Mechanics 1993;60(1):246–9.
[30] Anderson TL. Fracture mechanics – fundamentals and applications, Third Edition. Boca Raton, London, New York, Singapore: CRC Press, Taylor & Francis Group; 2005.
[31] Davidson BD, Krüger R, König M. Three-dimensional analysis of center-delaminated unidirectional and multidirectional single-leg bending specimens. Composites Science and Technology 1995;54:385–94.
[32] Rybicki EF, Kanninen MF. A finite element calculation of stress intensity factors by a modified crack closure integral. Engineering Fracture Mechanics 1977;9:931–8.
[33] Cicci D, Sharif F, Kortschot MT. Data reduction for the split cantilever beam mode III delamination test. In: Proceedings, ACCM 10, Whistler, British Columbia, Canada, 14–18 August 1995.

[34] Morais de A B. Transverse moduli of continuous-fibre-reinforced polymers. Composites Science and Technology 2000;60:997–1002.
[35] Morais de AB, Moura de MF, Marques AT, Castro de PT. Mode-I interlaminar fracture of carbon/epoxy cross-ply composites. Composites Science and Technology 2002;62:679–86.
[36] Szekrényes A, Uj J. Advanced beam model for fiber-bridging in unidirectional composite double-cantilever beam specimens. Engineering Fracture Mechanics 2005;72:2686–702.
[37] Szekrényes A, Uj J. Mode-II Fracture in E-glass/polyester Composite. Journal of Composite Materials 2005;39(19):1747–68.